2023 IEEE International Conference on Robotics and Automation (ICRA 2023)
May 29 - June 2, 2023. London, UK

Mapping Waves with an Uncrewed Surface Vessel via Gaussian Process Regression

Thomas M. C. Sears[1], M. Riley Cooper[1], and Joshua A. Marshall[1]

***Abstract*— Mobile robots are well suited for environmental surveys because they can travel to any area of interest and react to observations without the need for pre-existing infrastructure or significant setup time. However, vehicle motion constraints limit where and when measurements occur. This is challenging for a single vehicle observing a time-varying phenomenon, such as coastal waves, but the ability to generate a spatiotemporal map would have immediate scientific and engineering applications. In this paper, an uncrewed surface vessel (USV) was used to measure waves on the coast of Lake Ontario, Canada. Data were collected from a low-cost inertial measurement system onboard the USV and processed in an offline Gaussian process regression (GPR) workflow to create a spatiotemporal wave model. Frequency analysis of raw sensor data was used to best select and design kernel functions, and to initialize hyperparameters. The relative speed of the waves limited the ability to make complete wave reconstructions, but GPR captured the dominant periodic components of the waves despite irregularities in the signals. After optimization, the hyperparameters indicate a dominant signal with a wave period of 0.87 s, which concurs with ground truth estimates.**

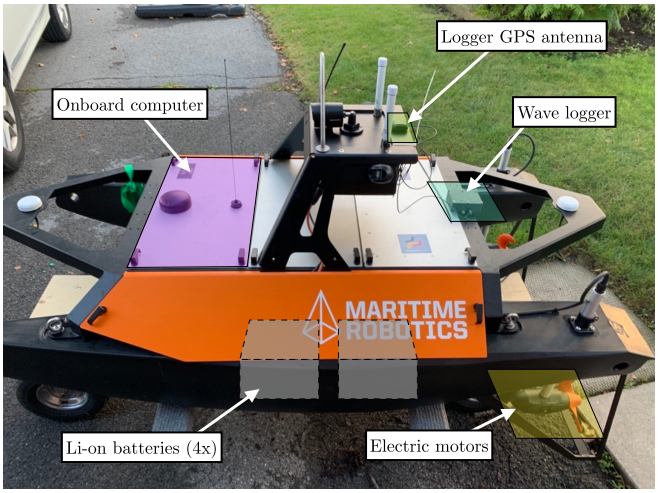

Fig. 1. Maritime Robotics Otter USV used in the field trials presented by this paper. The wave logger system is rigidly mounted at the rear of the USV and runs independently of the onboard computers and power systems.

I. INTRODUCTION

Roboticists have the opportunity to support vital environmental monitoring activities as societies strive to better understand, protect, and preserve natural ecosystems in a changing climate. For example, mobile robots can be deployed to support many of the United Nation's Sustainable Development Goals through data collection and modelling on land, in water, and in air [1]. Such field data is often obtained with an array of static sensors placed in an area under observation. Unfortunately, sensor installation(s) can be costly and time consuming, and changes to the desired measurement resolution or location would result in additional delays and expense. Field measurements can be made manually instead, which likely benefits the quality of the collected data as expertise and intuition provides real-time feedback to measurements, but such observations are limited by human factors: endurance, safety, and cost.

Mobile robots can collect this data instead because they can be utilized with minimal risk, without permanent infrastructure or upfront cost commitments, and still provide dynamic and flexible observations. Hardware advancements in ground, air, and marine robotics have led to mobile robot observers in many environmental monitoring applications [2], and now there is a need to develop the techniques and strategies that best use this data to model natural phenomena.

For unchanging environments, or environments with dynamics much slower than the survey speed of the robot, *spatial* models can be readily recreated from data. In contrast, this paper builds upon the work in [3] about modelling *spatiotemporal* phenomena with mobile robots by demonstrating these techniques for shallow water wave modelling in a lake. Field trials emulated the simulation experiment setup in [3] with an Otter uncrewed surface vessel (USV) off the coast of Kingston, Ontario, Canada in Lake Ontario. The USV was configured for tests as shown in Fig. 1. On-board inertial measurements were used to determine the off-normal rotation (i.e., the *tilt*) of the USV, which is a function of the scale and frequency of the traversed waves.

Observation datasets from a mobile robot in a dynamic environment are inherently sparse—the vehicle can not be in two places at once, nor monitor a single location for long durations without omitting measurements at other locations. It is therefore desirable to identify and leverage structures in the data, but to do so without being so specific that the modelling approach cannot adapt to a modified or new environment. A Gaussian process regression (GPR) workflow is proposed as a means to balance these competing interests. This allows the spatiotemporal mapping to remain generic, while specificity is established through the tuning of hyperparameters to match the observed data. GPR also evaluates prediction uncertainty, which can be used to assess model confidence or as a metric

*This project was funded in part by the NSERC Canadian Robotics Network (NCRN) and the Vanier Canada Graduate Scholarships Program.

[1]T. M. C. Sears, M. R. Cooper, and J. A. Marshall are all with the Department of Electrical & Computer Engineering and the Ingenuity Labs Research Institute, Queen's University at Kingston, Ontario, Canada, which is situated on the territory of the Haudenosaunee and the Anishinaabek. {thomas.sears,15mrc5,joshua.marshall}@queensu.ca

for robot path planning that focuses on improving model predictions [4], [5].

II. RELATED WORK

The desire to predict the past, present, and future of spatiotemporal phenomena has led to modelling developments with static and mobile sensors. Much work has been completed on the deployment of static sensors. With a non-uniformly distributed array of sites, Sahu and Mardia [6] demonstrated an ability to make spatiotemporal predictions of urban air pollution. At a smaller scale, indoor environmental monitoring was shown by Erickson *et al.* [7]. In both works, GPR was used to create three-dimensional spatiotemporal [6] and volumetric [7] maps. These works had the advantages of either pre-existing infrastructure or ease of sensor installation. This is in contrast to observations made in water, which is the application of focus in this paper.

Mobile sensors are more commonly found in challenging environments, such as marine surveys. Alam *et al.* [8] and Hansen *et al.* [9], [10] used uncontrolled aquatic sensors (so-called *drifters*) to monitor a coastal region. Because there is no ability to control a drifter, surveys require multiple vehicles to obtain a limited sample. Additionally, these works focused on relatively slow phenomena, so revisit times were not a concern. In Fossum *et al.* [11], an underwater uncrewed aquatic robot was deployed to sample phytoplankton. This survey was completed following a predetermined path, with the goal of generating a volumetric model of the phytoplankton. None of these studies considered the temporal dynamics because they were focused on slow-changing trends.

Spatiotemporal mapping with mobile robots has been previously proposed, but no work has fully demonstrated a flexible approach to observe and model a changing environment. Lan and Schwager [12] simulated spatiotemporal modelling with observations from multiple mobile sensors. This work was only in simulation and used *a priori* knowledge of the phenomenon to generate a model. Whitman *et al.* [13] proposed multiple mobile robot observers for simulated weed growth monitoring, where each robot could observe a limited area of interest. This work was also in simulation and used multiple vehicles with large sensing regions. Ma *et al.* [4] modelled a slow-changing phenomenon in real-time with measurements from a mobile robot by assuming the environment was static during robot observations. Experiments focused on pseudo-static phenomena and did not test the algorithms against fast changing fields. Singh *et al.* [14] used a moveable sensor to map a spatiotemporal field. This demonstrated GPR as a valid technique for spatiotemporal mapping in simulation and experiments, but the sensors were not subject to motion constraints often encountered with mobile vehicles.

A common thread in spatial and temporal mapping is the use of GPR as a modelling approach. Most often used to model a scalar field [6], [11], [7], [13], [4], [14], GPR has extensive heritage for use with mobile robotics and environmental observations. This work is mostly rooted in spatial modelling, so expanding our literature review beyond robotics provides more insight in to temporal modelling with GPR. For example, in Klenske *et al.* [15] a GPR model proved effective in mapping and, crucially, extrapolating predictions of behaviour for a control system. Senanayake *et al.* [16] similarly created a spatiotemporal model using GPR to predict seasonal variations of influenza. Common to both works is using a combination of covariance functions to capture long term and periodic trends.

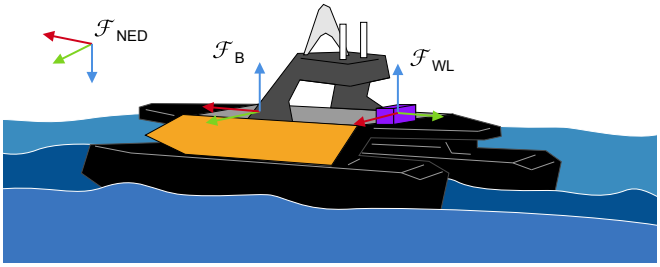

Fig. 2. Reference frames in wave mapping observations. $\mathcal{F}_{\text{NED}}$: local North-East-Down frame; $\mathcal{F}_{\text{B}}$: body-fixed boat frame, and; $\mathcal{F}_{\text{WL}}$: body-fixed wave-logger frame.

III. ROBOTIC WAVE MAPPING ON WATER

We demonstrate spatiotemporal mapping of coastal waves by using a mobile robot for data collection. Large scale coastal analysis is typically limited to wave spectrum information (e.g., see [17]), whereas a mobile sensor can be used to survey small and inaccessible areas to understand how wave formation occurs near the shore. Visual, radar [18], and inertial [19] wave measurement systems have all been demonstrated. Because mobile robots are often equipped with high performance navigation systems and could themselves benefit from a 'disturbance prediction' map of the waves, inertial measurements are proposed for this purpose.

A. Inertial Wave Measurements

When the USV crosses a wave, there will be a measurable change in the vehicle's roll and pitch. Measuring the wave angle is equivalent to calculating the transformation between the body-fixed USV frame $\mathcal{F}_{\text{B}}$ and the local North-East-Down frame $\mathcal{F}_{\text{NED}}$, because the water's surface is perpendicular to the local gravity vector (i.e., downward) at rest. Fig. 2 shows the relative orientation of these frames, as well as the frame of reference of the inertial measurement system $\mathcal{F}_{\text{WL}}$. After estimating the transformation $\boldsymbol{C}_{\text{NED,B}}$, such that

$$\mathcal{F}_{\text{NED}} = \boldsymbol{C}_{\text{NED,B}}\mathcal{F}_{\text{B}}, \tag{1}$$

$\boldsymbol{C}_{\text{NED,B}}$ can be decomposed into roll, pitch, and yaw Tait-Bryan angles.

Inertial sensors are well suited to wave observation because they can be stored within waterproof enclosures without affecting measurement accuracy. A gravity vector can be measured using a three-axis accelerometer and, in static applications, the trigonometric relation between the components can be used to find the overall tilt angle. This is less reliable for a moving USV because motor and wave forces are also measured by the accelerometer and, thus, skew the

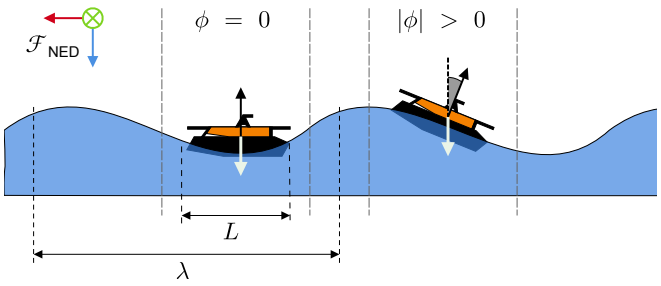

Fig. 3. Pitch and roll of the boat are a function of the wavelength, wave amplitude, and vessel length and width. At peaks and troughs, the boat normal will be collinear with the Down axis of the NED frame. Therefore, the direction of the gravity vector (white arrow) can be measured in the body-fixed frame in order to determine the wave angle ϕ.

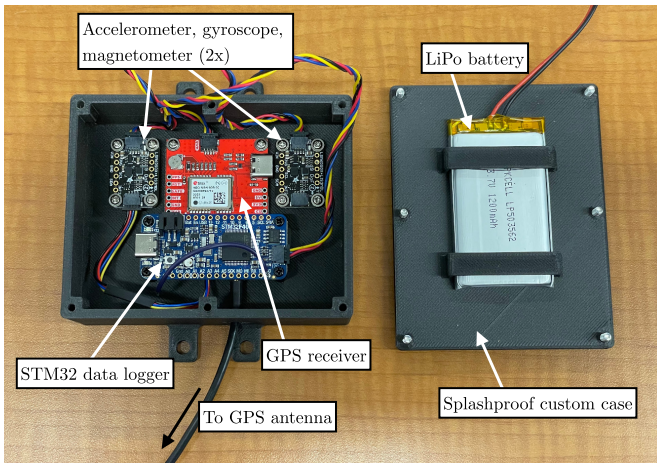

Fig. 4. Strap down wave logger system. Integrated memory and a battery allows the system to run independently of the USV and can be mounted wherever convenient.

result. Errors can be reduced by fusing additional sensors, such as a three-axis gyroscope, into the solution. This is the goal of attitude and heading reference systems (AHRS) that use accelerometer and gyroscope measurements to estimate attitude for mobile vehicles. In this paper, Madgwick's open-source orientation filter is used to determine $\boldsymbol{C}_{\text{NED,B}}$ [20]. The tilt angle ϕ, as illustrated in Fig. 3, is then

$$\phi = \arccos\left(\cos\left(\alpha\right)\cos\beta\right), \tag{2}$$

where α and β are the pitch (x) and roll (y) angles.

Limited access to real-time data from the Otter USV motivated the development of the *wave logger* system. This is a low-power, standalone system that uses commercial off the shelf components to record inertial motion data. The components are described in Tab. I and the integrated system is shown in Fig. 4. Two IMUs are used as they are low power and low cost. Gyroscope and accelerometer measurements by the two units are assumed to be independent, which provides a $\sqrt{2}$ noise reduction when averaged. The 1200 mAh LiPo battery provides more than 6 hours of runtime.

TABLE I
WAVE LOGGER COMPONENTS

Part	Description
STM32F405	Command and microSD card logging
LSM6DSOX + LIS3MDL	(2) Three-axis accelerometer, gyroscope, and magnetometer
NEO-M9N	GNSS receiver and SMA antenna
LiPo battery	3.7 V, 1200 mAh
Enclosure	Custom design and Markforged Onyx 3D print

B. Spatiotemporal Wave Mapping via GPR

A spatiotemporal wave map is generated as a batch process using all measurements through Gaussian process regression. $m \in \mathbb{Z}_{>0}$ observations are used to generate a mapping between training data inputs $\boldsymbol{X} = \{\boldsymbol{x}_i \mid i = 1, 2, ..., m\}$, where $\boldsymbol{x} \in \mathcal{X}$, $\mathcal{X} \subset \mathbb{R}^n$ is a vector of input values, and observation target values $\boldsymbol{y} = \{\hat{y}_i \mid i = 1, 2, ..., m\}$, $\hat{y} \in \mathcal{Y}$. For a mobile robot moving on water, vehicle pose and time of observation are chosen as the training data inputs; i.e., $\boldsymbol{x}_i = [x, y, t]_i$, where x and y are the vehicle position and t is the time of observation. By design, wave measurements are independent of vehicle heading, so it is omitted from the input data thus reducing the dimensionality of the mapping process from 4-D to 3-D.

A standard GPR formulation follows, which is thoroughly described in [21]. In short, the predicted distribution $\boldsymbol{f}_*$ is found as

$$\boldsymbol{f}_* | \boldsymbol{X}, \boldsymbol{y}, \boldsymbol{X}_* \sim \mathcal{N}\left(\bar{\boldsymbol{f}}_*, \text{cov}\left(\boldsymbol{f}_*\right)\right). \tag{3}$$

where

$$\bar{\boldsymbol{f}}_* \triangleq \mathbb{E}\left[\boldsymbol{f}_* | \boldsymbol{X}, \boldsymbol{X}_*\right] = \boldsymbol{\kappa}_* \left[\boldsymbol{\kappa} + \sigma_r^2 \boldsymbol{I}\right]^{-1} \boldsymbol{y}, \tag{4}$$

$$\text{cov}\left(\boldsymbol{f}_*\right) = \boldsymbol{\kappa}_{**} - \boldsymbol{\kappa}_* \left[\boldsymbol{\kappa} + \sigma_r^2 \boldsymbol{I}\right]^{-1} \boldsymbol{\kappa}_*, \tag{5}$$

$\boldsymbol{X}_*$ is the testing set, and $\boldsymbol{\kappa} \coloneqq \boldsymbol{\kappa}\left(\boldsymbol{X}, \boldsymbol{X}\right)$, $\boldsymbol{\kappa}_* \coloneqq \boldsymbol{\kappa}\left(\boldsymbol{X}_*, \boldsymbol{X}\right)$, and $\boldsymbol{\kappa}_{**} \coloneqq \boldsymbol{\kappa}\left(\boldsymbol{X}_*, \boldsymbol{X}_*\right)$ are a shorthand for the covariance function. Predictions are made with a test set of position-time pairs $\boldsymbol{X}_* = \{\boldsymbol{x}_{*,j} \mid j = 1, 2, ..., m_*\}$, $\boldsymbol{x}_{*,j} = [x_*, y_*, t_*]_j$. For an offline batch spatiotemporal mapping, $\boldsymbol{X}_*$ is selected to provide complete coverage of the region and duration of interest.

C. Covariance Function Design

Covariance functions (also known as *kernels*) quantify the correlation between two inputs, i.e., $\boldsymbol{\kappa}_{\text{ab}} \coloneqq \boldsymbol{\kappa}\left(\boldsymbol{x}_{\text{a}}, \boldsymbol{x}_{\text{b}}\right) : \mathcal{X} \times \mathcal{X} \to \mathbb{R}$. When properly tuned in a GPR, each function can capture a trend in the data across an input dimension. If multiple trends are anticipated, covariance functions can be the sum $\boldsymbol{\kappa}_{\text{ab,SUM}} = \boldsymbol{\kappa}_{\text{ab},1} + \boldsymbol{\kappa}_{\text{ab},2} + \cdots + \boldsymbol{\kappa}_{\text{ab},k}$, the product $\boldsymbol{\kappa}_{\text{ab,PROD}} = \boldsymbol{\kappa}_{\text{ab},1}\boldsymbol{\kappa}_{\text{ab},2} \ldots \boldsymbol{\kappa}_{\text{ab},k}$, or even combinations of combinations of covariance functions. Although it is appealing to select many covariance functions to capture all possible trends, designers must consider the increased optimization times and the potential for overfitting.

Selecting appropriate covariance functions can be challenging without *a priori* knowledge about the structure of the phenomenon, but general trends can be anticipated

and accounted for. Note that automatic covariance function selection is an area of research; see [22].

Correlations between inputs that are 'nearby' can be captured by the squared exponential kernel

$$\boldsymbol{\kappa}_{\text{ab,SE}} = \exp\left[-\frac{1}{2}\left(\boldsymbol{x}_a - \boldsymbol{x}_b\right)^{\mathsf{T}} \boldsymbol{L}_{\text{SE}} \left(\boldsymbol{x}_a - \boldsymbol{x}_b\right)\right] \tag{6}$$

where $\boldsymbol{L}_{\text{SE}} = \text{diag}\left(\boldsymbol{l}_{\text{SE}}^{-2}\right)$ are the lengthscale hyperparameters. $\boldsymbol{l}_{\text{SE}} \in \mathbb{R}^3$ weights the correlation between inputs relative to their Euclidean distance in any axis (space or time), so a larger $\boldsymbol{l}$ increases correlation to points farther away. A combination of squared exponential kernels can be used to capture short, medium, and long term trends [21]. In wave modelling, long baseline correlations are expected to be perpendicular to the wave direction

When data correlations are expected to have repeating structures, MacKay [23] proposed a form of periodic covariance function, given by

$$\boldsymbol{\kappa}_{\text{ab,Per}} = \exp\left[-2\sin^2\left(\pi \boldsymbol{P}\left(\boldsymbol{x}_a - \boldsymbol{x}_b\right)\right) \boldsymbol{L}_{\text{Per}}\right] \tag{7}$$

where $\boldsymbol{P} = \text{diag}\left(\boldsymbol{T}^{-1}\right)$ and $\boldsymbol{T} \in \mathbb{R}^3$ is the period hyperparameter, and $\boldsymbol{L}_{\text{Per}} = \text{diag}\left(\boldsymbol{l}_{\text{Per}}^{-2}\right)$, $\boldsymbol{l}_{\text{Per}} \in \mathbb{R}^3$ is the lengthscale. The periodic covariance function strongly correlates inputs separated by $|x_{a,k} - x_{b,k}| = T_k$. With multiple periodic kernels, multiple frequencies of signals can be captured.

The GPR formulation previously discussed assumes a zero-mean signal. For a spatiotemporal map of the wave surface angle, specifically measured as the magnitude of the pitch and roll between the USV and the local gravity vector, the mean will be non-zero. A bias covariance function could be added, but this is omitted because the periodic kernel provides correlations beyond the sampled space and time.

The Python `GPy` library [24] was utilized in this work (`GPy` v1.10.0, `python` v3.10.4). This library provides squared exponential and a periodic covariance function implementations and the ability to combine covariance functions across multiple input dimensions.

D. Covariance Function Selection

The covariance functions used in a GPR workflow are selected to best recreate latent structures in the data. Selection is primarily restricted by available compute, as each covariance function introduces hyperparameters that increase optimization time, but designer creativity in selecting suitable functions can also be a limiting factor. For coastal water waves there is an expectation that repeating structures will be present along the time dimension and perpendicular to the wave direction, so we desire a strongly repeating covariance function. There is a consistency in the data parallel to the wave direction, so strong correlations are required in this dimension. Multiple covariance functions were selected for each axis to capture long, short, and periodic trends. A 'product of sums' was ultimately selected, i.e.,

$$\begin{aligned}\boldsymbol{\kappa}_{\text{All}} = &\left[\boldsymbol{\kappa}_{\text{SE}}^{\text{L}} + \boldsymbol{\kappa}_{\text{SE}}^{\text{S}} + \boldsymbol{\kappa}_{\text{Per}}^{\text{L}} + \boldsymbol{\kappa}_{\text{Per}}^{\text{S}}\right]_x \cdots \\ &\left[\boldsymbol{\kappa}_{\text{SE}}^{\text{L}} + \boldsymbol{\kappa}_{\text{SE}}^{\text{S}} + \boldsymbol{\kappa}_{\text{Per}}^{\text{L}} + \boldsymbol{\kappa}_{\text{Per}}^{\text{S}}\right]_y \cdots \\ &\left[\boldsymbol{\kappa}_{\text{SE}}^{\text{L}} + \boldsymbol{\kappa}_{\text{SE}}^{\text{S}} + \boldsymbol{\kappa}_{\text{Per}}^{\text{L}} + \boldsymbol{\kappa}_{\text{Per}}^{\text{M}} + \boldsymbol{\kappa}_{\text{Per}}^{\text{S}}\right]_t\end{aligned} \tag{8}$$

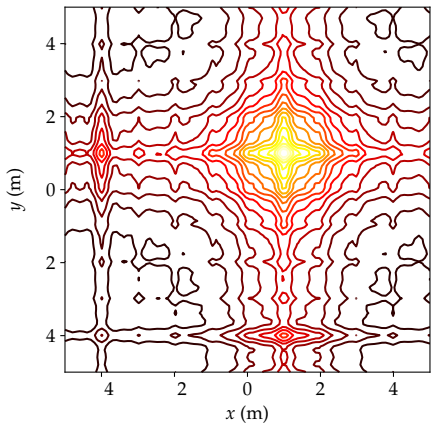

Fig. 5. Contour plot of $\boldsymbol{\kappa}_{\text{All}}$ covariance function across x-y input space. Correlation is highest in the yellow regions and are compared against a point at $(1, 1, 0)$. High correlations repeat along an x-y oriented grid.

where L, M, and S functions target long, medium, and short lengthscales or periods. This composite function has a total of 34 hyperparameters. The motivation for multiple periodic functions is to try to capture the dominant signals in irregular water waves.

Visualizations can be powerful tools to understand covariance function choice at higher dimensions [25]. $\boldsymbol{\kappa}_{\text{All}}$ is shown across two input dimensions (x and y spatial axes) in Fig. 5. This is before optimization, but it shows that the combined kernel function meets our design intentions and that it may be capable of extrapolating waves measurements to space and time not observed.

IV. USV FIELD TRIALS

Field experiments were performed with an Otter USV, a modular marine robot manufactured by Maritime Robotics.

A. Experimental Apparatus and Setup

The Otter USV is an autonomous robotic catamaran designed for sonar and bathymetric scanning with onboard GPS and IMU sensors. The USV measures 2.00 m by 1.08 m by 0.815 m and is suitable for use in 50 cm high coastal waves. Refer back to Fig. 1 for the as-tested configuration of the USV.

An on-shore laptop runs the manufacturer's proprietary vehicle control software (VCS) and communicates with the USV over a long range Wi-Fi connection. The VCS can be used to create custom paths for the vehicle to follow. After loading a custom path, the USV operates independently of the VCS, performing navigation and control calculations onboard. Despite having capable GPS and IMU sensors for these purposes, the existing software limits external access and logging of these parameters to 5 Hz, which was considered too slow for wave mapping.

Testing was performed off the shore of Lake Ontario in Kingston, Ontario, Canada (Lat: 44.2180, Long: –76.5104). Direction of travel of waves was observed to be approximately north-east for the duration of the test. The relative position and orientation of the vehicle, test path, and wave

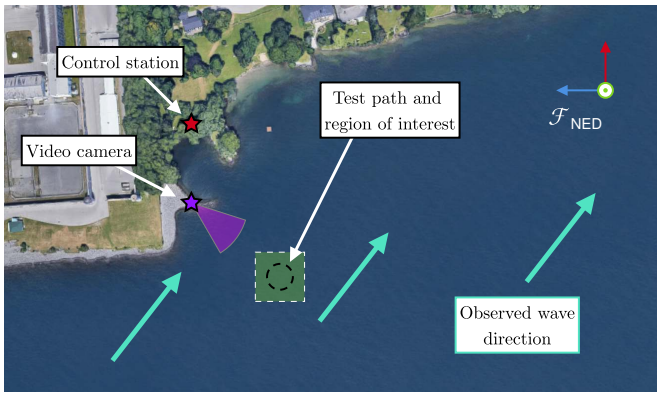

Fig. 6. Measurement path (black dashed line) as planned in the VCS. Approximate average range from the control station to USV was 200 m. Waves were travelling in a north-east direction, so trial video recordings face south-east to best observe wave motion.

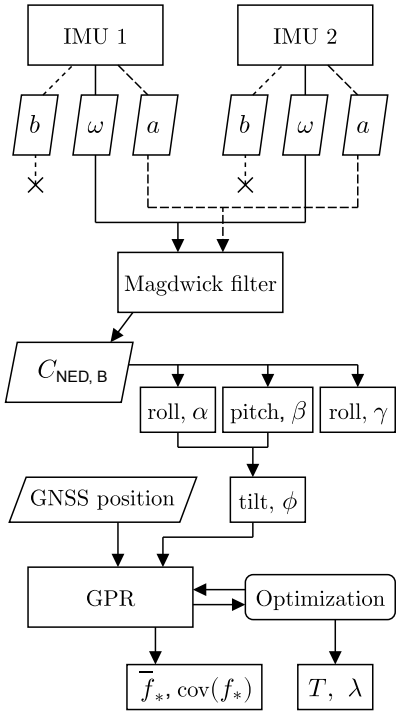

Fig. 7. Processes and data required to transform wave logger data into a spatiotemporal wave model.

direction are shown in Fig. 6. The USV followed the charted circular path in a counter-clockwise direction beginning on the easternmost waypoint. The USV was allowed to run autonomously for four minutes and collected dual-IMU and GPS data at 10 Hz.

B. Results

Data from the wave logger was processed according to Fig. 7 to obtain a spatiotemporal model of the waves. Over 2000 data points were collected over a four minute trial.

Experiments were completed without ground truth observations that can provide accurate estimates of wave height, period, or wavelength. Instead, an order-of-magnitude assessment of the spatiotemporal mapping accuracy was established with an additional dataset collected while the USV was set in station-keeping mode. In this mode, the USV attempts to maintain a constant position and heading. By holding position constant, time becomes the only input and allows for a measurement of wave period at this point. Frequency analysis of z accelerations and x gyroscope measurements are shown in Fig. 8. These measurements were selected as they are the least likely to be effected by motor activity, which are in a fixed configuration parallel with the USV's x-axis. The results show a concentration of energy in both signals around 1 Hz. These data also matched a manual wave count from field trial video recordings, in which wave crests were counted for a fix time, but this count is subject to significant variation because of lighting and the irregularity of the waves.

TABLE II
HYPERPARAMETER OPTIMIZATION AND RESULTS.

Parameters	Direction	Initial Value	Final Value
Squared Exponential l_{SE}	x	10.0 1.0	2.62 0.41
	y	10.0 1.0	4.37 0.35
	t	10.0 1.0	3.27 2.19
Periodic T	x	5.0 1.0	0.75 0.42
	y	5.0 1.0	0.46 0.46
	t	2.0 1.0 0.5	1.74 0.92 0.92

A quantitative assessment of the mapping accuracy can be made by comparing GPR period hyperparameters after optimization, as shown in Tab. II, to the stationkeeping baseline wave period. We identify the dominant periodic covariance function as that with the largest variance hyperparameter, which is T_t^{long}. This had a final value of $T_t^{\text{long}} = 1.74$, which can be directly translated into the time dimension as a period, or 1.74 s. This closely matches the expected 1 Hz signal as the spatiotemporal scalar field is predicting tilt magnitude, which will have double the frequency of the waves.

For a qualitative understanding of the spatiotemporal performance, we can directly view a recreation of the shallow water waves. Fig. 9 shows a snapshot of the wave map at the end of the survey. The periodic trends in the data are only leveraged in the region nearest the USV. This limits the models ability to make wide reaching predictions, but local modelling may still be possible. However, as discussed in [3], the optimization process can be difficult with this type of sparse data set. Creating a coherent prediction, even if only useful in a local region, is a beneficial outcome.

V. CONCLUSIONS

The experiments completed in this work successfully extended previous developments toward spatiotemporal mod-

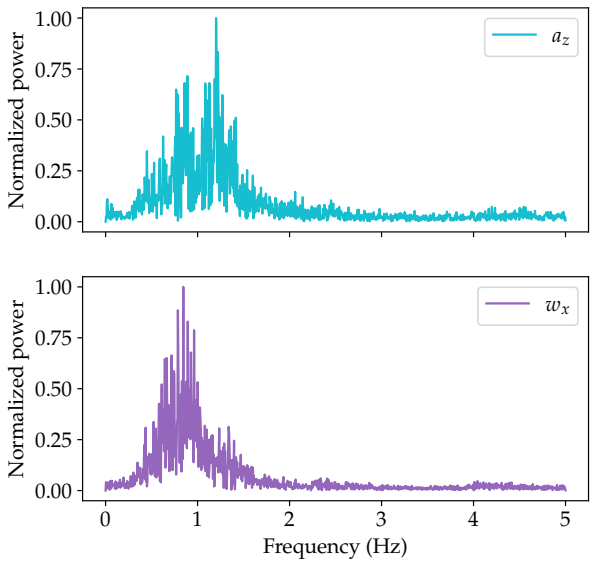

Fig. 8. Frequency distribution of acceleration (a_z) and angular velocity (ω_x) measurements as measured by the wave logger IMU. These axes of measurement are considered for their minimal sensitivity to motor thrust. 10 Hz sampling is sufficiently fast to capture the entire wave frequency spectrum.

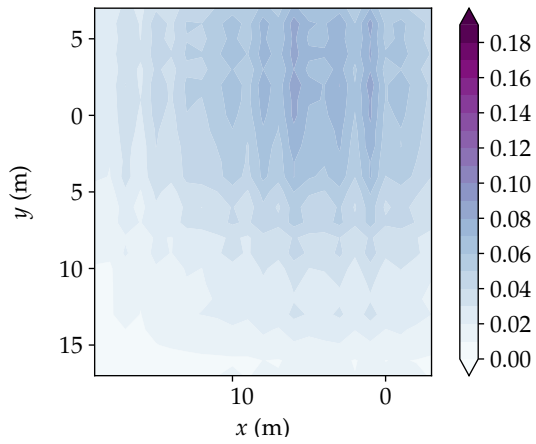

Fig. 9. Spatiotemporal wave map at $t = 240$ s, as generated with inertial motion wave logger data through Gaussian process regression.

elling with data from mobile robots. An uncrewed surface vessel was equipped with a low-cost inertial motion logging system to collect measurements of the magnitude of the slope of the waves. Data collected from a four-minute observation campaign while driving through coastal waves were used in a spatiotemporal modelling workflow that uses Gaussian process regression to make predictions at locations and times never visited. Covariance functions were carefully selected to suit the expected dynamics, but left generic to not oversimplify the problem. After optimization, key hyperparameters matched wave predictions from additional datasets and video recordings of the lake during the trial. Experiments did not include a rigorous ground truth, so the complete spatiotemporal model cannot be directly assessed. Qualitative results indicate the model could capture periodic trends, but had difficulty predicting the non-orthogonal wave direction due to limitations in the Gaussian process implementation.

While the developments presented in this paper are promising, further experimentation is needed to fully grasp the capabilities and limits of the demonstrated mapping workflow. Future work will explore the capabilities of the spatiotemporal GPR modelling workflow in a range of real and simulated wave conditions. This will provide a necessary understanding to the limits of this modelling method as well as whether it is suitable for real-time operation. For future field trials, performance will be assessed against ground truth established from drone video footage and in-situ static sensors. As modelling is currently a batch approach, scalability of this spatiotemporal mapping technique requires further attention, as larger datasets collected over longer periods will become difficult to manage and impossible to run in real-time on a USV.

In taking this work beyond environmental monitoring, spatiotemporal disturbance modelling can be used to improve robot control in dynamic environments. In marine applications, the presented wave slope map could provide predictions of the future wave conditions such that the autonomous vehicle could avoid, pre-empt, or exploit the coming disturbance.

References

[1] United Nations Department of Economic and Social Affairs - Sustainable Development. The 17 goals. (accessed: 09-2022). [Online]. Available: https://sdgs.un.org/goals

[2] M. Dunbabin and L. Marques, "Robots for environmental monitoring: Significant advancements and applications," *IEEE Robotics Automation Magazine*, vol. 19, no. 1, pp. 24–39, Mar. 2012.

[3] T. M. C. Sears and J. A. Marshall, "Mapping of spatiotemporal scalar fields by mobile robots using Gaussian process regression." in *Proceedings of the 2022 IEEE/RSJ International Conference on Intelligent Robots and Systems (IROS)*, Kyoto, Japan, Oct. 2022, to be published.

[4] K.-C. Ma, L. Liu, and G. S. Sukhatme, "Informative planning and online learning with sparse Gaussian processes," in *Proceedings of the 2017 IEEE International Conference on Robotics and Automation (ICRA)*, May 2017, pp. 4292–4298.

[5] K.-C. Ma, L. Liu, H. K. Heidarsson, and G. S. Sukhatme, "Data-driven learning and planning for environmental sampling," vol. 35, no. 5, pp. 643–661.

[6] S. K. Sahu and K. V. Mardia, "A Bayesian kriged Kalman model for short-term forecasting of air pollution levels," *Journal of the Royal Statistical Society: Series C (Applied Statistics)*, vol. 54, no. 1, pp. 223–244, Jan. 2005.

[7] P. Erickson, M. Cline, N. Tirpankar, and T. Henderson, "Gaussian processes for multi-sensor environmental monitoring," in *Proceedings of the 2015 IEEE International Conference on Multisensor Fusion and Integration for Intelligent Systems (MFI)*, Sep. 2015, pp. 208–213.

[8] T. Alam, G. M. Reis, L. Bobadilla, and R. N. Smith, "A data-driven deployment approach for persistent monitoring in aquatic environments," in *Proceedings of the 2018 Second IEEE International Conference on Robotic Computing (IRC)*, Jan. 2018, pp. 147–154.

[9] J. Hansen, S. Manjanna, A. Q. Li, I. Rekleitis, and G. Dudek, "Autonomous marine sampling enhanced by strategically deployed drifters in marine flow fields," in *Proceedings of OCEANS 2018 MTS/IEEE Charleston*, 2018, pp. 1–7.

[10] J. Hansen and G. Dudek, "Coverage optimization with non-actuated, floating mobile sensors using iterative trajectory planning in marine flow fields," in *Proceedings of the 2018 IEEE/RSJ International Conference on Intelligent Robots and Systems (IROS)*, 2018, pp. 1906–1912.

[11] T. O. Fossum, G. M. Fragoso, E. J. Davies, J. E. Ullgren, R. Mendes, G. Johnsen, I. Ellingsen, J. Eidsvik, M. Ludvigsen, and K. Rajan, "Toward adaptive robotic sampling of phytoplankton in the coastal ocean," *Science Robotics*, vol. 4, no. 27, p. eaav3041, Feb. 2019.

[12] X. Lan and M. Schwager, "Learning a dynamical system model for a spatiotemporal field using a mobile sensing robot," in *Proceedings of the 2017 American Control Conference (ACC)*. Seattle, WA, USA: IEEE, May 2017, pp. 170–175.

[13] J. E. Whitman, H. Maske, H. A. Kingravi, and G. Chowdhary, "Evolving gaussian processes and kernel observers for learning and control in spatiotemporally varying domains: With applications in agriculture, weather monitoring, and fluid dynamics," *IEEE Control Systems Magazine*, vol. 41, no. 1, pp. 30–69, Feb. 2021.

[14] A. Singh, F. Ramos, H. D. Whyte, and W. J. Kaiser, "Modeling and decision making in spatio-temporal processes for environmental surveillance," in *Proceedings of the 2010 IEEE International Conference on Robotics and Automation*, May 2010, pp. 5490–5497.

[15] E. D. Klenske, M. N. Zeilinger, B. Schölkopf, and P. Hennig, "Gaussian process-based predictive control for periodic error correction," *IEEE Transactions on Control Systems Technology*, vol. 24, no. 1, pp. 110–121, Jan. 2016.

[16] R. Senanayake, S. O'Callaghan, and F. Ramos, "Predicting spatio-temporal propagation of seasonal influenza using variational gaussian process regression," *Proceedings of the 2016 AAAI Conference on Artificial Intelligence*, vol. 30, no. 1, Mar. 2016.

[17] C. McLaughlin, B. Law, and R. Mulligan, "Modeling surface waves and tide–surge interactions leading to enhanced total water levels in a macrotidal bay," *Coastal Engineering Journal*, vol. 64, no. 1, pp. 24–41, 2022.

[18] L. Szczyrba, "Imaging coastal waves with radar," *Nature Reviews Earth & Environment*, vol. 3, no. 7, pp. 423–423, Jul. 2022.

[19] J. Rabault, T. Nose, G. Hope, M. Müller, O. Breivik, J. Voermans, L. R. Hole, P. Bohlinger, T. Waseda, T. Kodaira, T. Katsuno, M. Johnson, G. Sutherland, M. Johansson, K. H. Christensen, A. Garbo, A. Jensen, O. Gundersen, A. Marchenko, and A. Babanin, "OpenMetBuoy-v2021: An Easy-to-Build, Affordable, Customizable, Open-Source Instrument for Oceanographic Measurements of Drift and Waves in Sea Ice and the Open Ocean," *Geosciences*, vol. 12, no. 3, p. 110, Mar. 2022.

[20] S. O. H. Madgwick, A. J. L. Harrison, and R. Vaidyanathan, "Estimation of IMU and MARG orientation using a gradient descent algorithm," in *Proceedings of the 2011 IEEE International Conference on Rehabilitation Robotics*, Jun. 2011, pp. 1–7.

[21] C. E. Rasmussen and C. K. I. Williams, *Gaussian Processes for Machine Learning*, ser. Adaptive Computation and Machine Learning. Cambridge, MA: MIT Press, 2006.

[22] D. Duvenaud, J. Lloyd, R. Grosse, J. Tenenbaum, and G. Zoubin, "Structure discovery in nonparametric regression through compositional kernel search," in *Proceedings of the 2013 International Conference on Machine Learning*. PMLR, 2013, pp. 1166–1174.

[23] D. J. MacKay *et al.*, "Introduction to Gaussian processes," *NATO ASI series F computer and systems sciences*, vol. 168, pp. 133–166, 1998.

[24] GPy, "GPy: A Gaussian process framework in python," http://github.com/SheffieldML/GPy, since 2012.

[25] D. Duvenaud, "Automatic model construction with Gaussian processes," Ph.D. dissertation, Computational and Biological Learning Laboratory, University of Cambridge, 2014.